CrystEngComm

Accepted Manuscript

ROYAL SOCIETY OF CHEMISTRY

www.rsc.org/crystengcomm

PAPER www.rsc.org | CrystEngComm

Synthesis and Lithium Storage Performance of Nickel Oxide Octahedra

Zheng Kun Yang,[a,b] Le Xin Song,[a,b,c]*, Rong Rong Xu,[b] Yue Teng,[b,c] Juan Xia,[b,c] Li Zhao[b] and Qing Shan Wang[b]

The present work was devoted to the construction of nickel oxide (NiO) polyhedral structures through a simple, efficient and environmentally friendly one-step process. Initially, a series of intimate mixtures of nickel chloride ($NiCl_2$) and β-cyclodextrin (β-CD) with different initial molar ratios were used as precursors. By simply sintering the precursors, we successfully obtained NiO octahedra with smooth surface and uniform size distribution. Control experiments showed the formation, morphology and grain size of NiO octahedra can be finely modulated by changing two parameters: the initial molar ratio of $NiCl_2$ to β-CD and the sintering time. The former is a decisive factor for creating the NiO octahedra, while the latter is a key factor for regulating their size and shape evolution. Moreover, we found that the role of β-CD can be played, but less well, by other carbon sources such as active carbon and glucose. Several independent experiments (FTIR spectra, conductivity and thermogravimetric analyses) were done to understand the mechanism of this role. Our data suggested that β-CD produced a stronger interaction with $NiCl_2$ than the other two carbon sources, leading to an earlier transformation from $NiCl_2$ to NiO. Further, this octahedral material exhibited a very small hysteresis loop below 1000 Oe at 300 K, indicating ferromagnetic behaviour, which is different from the antiferromagnetic behaviour of bulk NiO materials. Electrochemical tests demonstrated that the octahedral structure as well as an agglomerate structure has high lithium storage capacity. Also, the agglomerate structure presented very low irreversible capacity loss and good cyclability. Therefore, it gives an impression that they are promising anode materials of rechargeable lithium-ion batteries, for high power applications in particular. We believe that these results will increase our understanding of the relationship between structures, properties and functions of transition metal oxide materials.

1. Introduction

Nickel oxide (NiO) is a material that has been the subject of a considerable number of research efforts due to its unique electrical and magnetic properties.[1–3] The formation of various NiO nanostructures such as nanopolyhedra,[4] nanotubes,[5] nanowires,[6] nanoflakes,[7] nanorings,[8] nanospheres,[9] nanorods[10] and nanoflowers[11] was reported in the past. These nanostructures can be created by various methods such as solvothermal and hydrothermal synthesis,[12] chemical vapor deposition,[4] and sonochemical[13] and electrodeposition processes.[14] However, these methods have at least one of the following limitations: i) involvement of multiple steps, ii) need of stabilizers, iii) using organic solvents and iv) with templates. Therefore, simple, effective and environmentally friendly synthesis procedures are still in demand.

On the other hand, lithium-ion batteries for electrochemical energy storage and conversion have received wide attention due to their high power and energy density in the past decades.[15,16] They have been dominant power sources for portable electronic devices such as digital cameras, handheld computers and mobile phones. With the fast development of electronic products, there is a continuous increasing demand for higher energy capacity, better cycling performance and longer cycle life. In order to meet the demand, the development of higher performance electrode materials is necessary. Among the available materials, transition metal oxides are believed to have a promising advantage owing to their physical and chemical characteristics. As a result, numerous transition metal oxides with various morphologies and sizes, such as TiO_2 nanotubes,[17] V_2O_5 nanosheets,[18] MoO_3 nanobelts[19] and Co_3O_4 nanoneedles,[20] have also been tested as possible candidates for lithium-ion battery materials. Also, there have been many reviews about the merits and shortcomings of the materials in lithium-ion batteries.[21] Therefore, it is an interesting and open challenge to understand the relationship between the structure and the activity of transition metal oxides in lithium-ion batteries. Recently, various kinds of nanostructures of NiO like nanoflowers,[22,23] nanosheets[24–26] and nanowires[27] were used as the anode material for lithium-ion batteries, showing remarkable discharge capacity, and enhanced cycling stability. However, hitherto, there have been few reports on the comparison of electrochemical performance between polyhedra and other structures of NiO.

Taking these into consideration, the present study makes an initial attempt to construct polyhedral NiO by a simple and environmentally friendly approach, and to compare its activity in lithium-ion batteries, with those of other nanostructures.

Initially, we prepared a group of binary mixtures consisting of nickel chloride ($NiCl_2$) with β-cyclodextrin (β-CD) by simply mixing them in water using different molar ratios. Subsequently, two kinds of NiO microstructure materials: octahedral structure and agglomerate structures were successfully obtained by directly sintering the binary mixtures. Two key parameters: the concentration of β-CD and the sintering time were determined to play an important role in control of size and shape of NiO materials. Finally, a comparison of the electrochemical results demonstrated that one of the agglomerate structures with excellent electrochemical performance is a potential anode material for next generation lithium-ion batteries.

In short, this study provides the first report of successful growth of NiO octahedra and agglomerates by β-CD-assisted one-pot synthesis, and gives insight into the relation between the structure and function of the materials. It can be predicted that this powerful synthesis strategy will be widely applied in the future.

2. Experimental

2.1 Materials

β-CD and $NiCl_2{\cdot}6H_2O$ were purchased from Shanghai Chemical Reagent Company. Glucose was bought from China Pharmacy Group (Shanghai, China). They were directly used as received without further purification. Commercial active carbon was obtained from Sinopharm Chemical Reagent Co. Ltd. (Shanghai, China). All other reagents are of analytical-reagent grade, unless stated other-

[a]*Division of Nanomaterials and Chemistry, Hefei National Laboratory for Physical Sciences at Microscale, University of Science and Technology of China, Hefei 230026, P. R China*
[b]*Department of Chemistry, University of Science and Technology of China, Hefei 230026, P. R China*
[c]*CAS Key Laboratory of Materials for Energy Conversion, Department of Materials Science and Engineering, University of Science and Technology of China, Jin Zhai Road 96, Hefei 230026, P. R China*
Email: solexin@ustc.edu.cn;
Fax: +86-551-63601592; Tel: +86-551-63492002

wise.

2.2 Preparation of the intimate mixtures of *β*-CD and $NiCl_2$

In a typical experiment, $NiCl_2·6H_2O$ (1 mmol, 0.237 g) with *β*-CD (0.1 mmol, 0.113 g) were dissolved in 60 mL deionized water, and stirred at 333 K for 6 h in a round-bottom flask. After water was removed by rotary evaporation under vacuum (76 Torr) below 323 K, a green product was obtained and dried in vacuo at 333 K for 24 h to remove water from the solid. Subsequently, the green powder (named as $NiCl_2$-*β*-CD-**a**) was kept in an evacuated desiccator over P_2O_5 until further use. Two other intimate mixtures of $NiCl_2$ and *β*-CD with the initial molar ratios (IMRs) of 1:1 ($NiCl_2$-*β*-CD-**b**), 1:10 ($NiCl_2$-*β*-CD-**c**), as well as the mixtures of $NiCl_2$ with active carbon ($NiCl_2$-carbon) and glucose ($NiCl_2$-glucose) with the IMR of 10:1, were prepared with the same general procedure.

2.3 Preparation of NiO crystals

NiO-**1a**, NiO-**2** and NiO-**3** were prepared by sintering $NiCl_2$-*β*-CD-**a**, -**b** and -**c** at the temperature of 773 K in a muffle furnace for 12 h in air, respectively. NiO-**1b**, -**1c** and -**1d** were prepared by sintering $NiCl_2$-*β*-CD-**a** at the same temperature but with different sintering times: 2, 4 and 8 h respectively in air to investigate the crystal growth process. NiO-**4** and -**5** were prepared by sintering $NiCl_2$-carbon and $NiCl_2$-glucose respectively at the same conditions as the NiO-**1**. After sintering, the NiO samples were slowly cooled to room temperature and kept in an evacuated desiccator over P_2O_5 until further use.

The result of flame atomic absorption spectrometry (FAAS) for two representative agglomerates, NiO-**1b** and NiO-**3**: Calcd. for NiO: Ni, 78.57%; Found for NiO-**1b**: Ni, 78.59% and for NiO-**3**: Ni, 78.58%. X-ray energy dispersive spectrometry (EDS) analyses for a point of a single agglomerate (Figs. S1 and S2, ESI†) indicated that the molar ratios of Ni to O are 1.00:1 in NiO-**1b** and 1.06:1 in NiO-**3**, respectively. These results demonstrated the high purity of the agglomerate materials.

2.4 Electrochemical tests

Electrodes for electrochemical studies were prepared by mixing 70 wt% the as-obtained NiO crystals, 20 wt% conducting acetylene black, and 10 wt% carboxymethyl cellulose in water. The slurry was pasted on a clean copper foil, and dried in vacuo at 373 K for 12 h. Subsequently, the coated foil was roll-pressed and cut into a round slice. Test cells were assembled in an argon-filled glove box using lithium foil as the counter electrode and the reference electrode, Celgard 2400 as the separator, and a mixed solution of $LiPF_6$ (1 $mol·dm^{-3}$) with ethylene carbonate, ethyl methyl carbonate and dimethyl carbonate (1:1:1, v/v/v) as electrolyte. The cells were charged and discharged from 0.01 to 3.00 V at the current density of 100 $mA·g^{-1}$ with a LAND CT2001A cell test instrument.

2.5 Instruments and measurements

X-ray diffraction (XRD) patterns of solid samples were recorded in a Philips X' Pert Pro X-ray diffractometer. Samples were irradiated with monochromatized Cu Kα and analyzed with $20° \le 2\theta \le 90°$. Tube voltage and current were 40 kV and 40 m A, respectively.

Crystal morphologies of samples were observed with a Supra 40 field-emission scanning electron microscopy (FE-SEM) operated at 5 kV. Transmission electron microscopy (TEM) images were obtained with a JEOL-2010 microscope using an accelerating voltage of 200 kV. High-resolution transmission electron microscopy (HR-TEM) images were taken on a JEOL-2010 microscope at an accelerating voltage of 200 kV. The composition of samples was determined by EDS analysis attached to the FE-SEM instrument. FAAS was performed using an atomic absorption spectrophotometer AAnalyst 800 (Perkin-Elmer, USA).

Conductivity was measured at 298 K using a Leici DDSJ-308 conductivity meter (Leici Instrument Factory, Shanghai, China) with automatic temperature compensation and automatic calibration. A conductance cell with a cell constant of 0.984 cm^{-1} was used in a water bath whose temperature was kept at 298 K.

FTIR spectra were recorded on a Bruker Equinox 55 spectrometer with KBr pellets in the range of 400–4000 cm^{-1} with a resolution of 0.5 cm^{-1}. Raman spectra were obtained with a LABRAM-HR Confocal Laser MicroRaman spectrometer with 785.0 nm laser excitation in the range 500–2000 cm^{-1} with a resolution of 0.6 cm^{-1} at room temperature.

Thermogravimetric (TG) analyses were conducted using a Shimadzu TGA-50 (Shimadzu, Tokyo, Japan) analyser with temperature programmed at a constant heating rate of 10.0 $K·min^{-1}$ under a nitrogen atmosphere with a gas flow of 25 $mL·min^{-1}$.

Magnetic measurements of samples were carried out on a Quantum Design (QD, San Diego, USA) Magnetic Property Measurement System (MPMS-7XL) equipped with a SQUID by means of a vibrating sample magnetometer.

3. Results and discussion

3.1 Structure and morphology of NiO-1a

Fig. 1 shows the XRD pattern of NiO-**1a**. All the diffraction peaks can be clearly indexed to a face-centered cubic structure of NiO (JCPDS 73-1519, S.G.: $Fm\bar{3}m$).[28] The characteristic peaks at 2θ angles of 37.2, 43.2, 62.8, 75.3 and 79.5° correspond to (111), (200), (220), (311) and (222) of cubic NiO, respectively. No impurity peaks are detected.

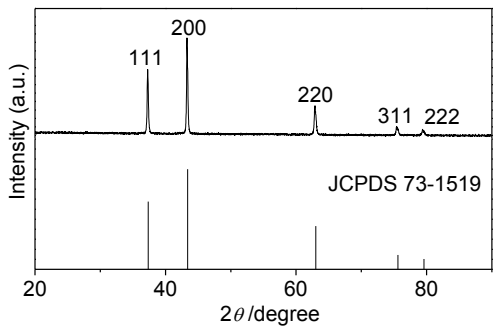

Fig. 1 XRD pattern of NiO-**1a** prepared by sintering $NiCl_2$-*β*-CD-**a**

Fig. 2a displays the FE-SEM image of the NiO-**1a**. Clearly, the octahedra consisting of 8 equilateral triangular surfaces and 12 identical edges (with a mean edge length of 400~500 nm) have relatively uniform and well-defined properties (Fig. S3, ESI†) The HR-TEM image in Fig. 2b shows a lattice spacing of 0.24 nm, corresponding to the (111) place of fcc NiO,[29] which is consistent with the XRD analysis. Moreover, the highly ordered structure is further proved by the TEM image in the inset of Fig. 2b. The NiO octahedra were originated from the sintering of $NiCl_2$-*β*-CD-**a** with the IMR of

10:1. Therefore, we hope to understand what are the role of β-CD and the effect of sintering parameters.

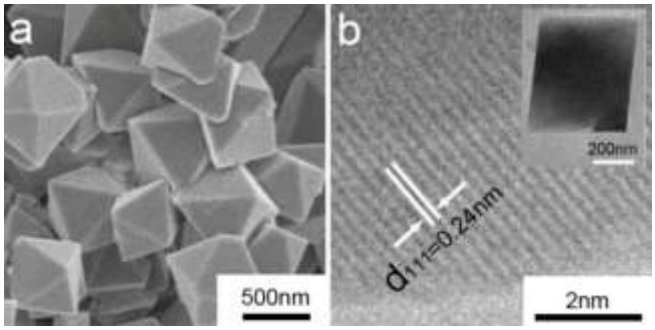

Fig. 2 FE-SEM image (a), HR-TEM image (b) of NiO-**1a**. The inset in (b) is the TEM image of a single octahedron.

3.2 Formation of NiO-1a

Control experiments indicate that the formation of the octahedral NiO structure is indeed related to the preparation conditions such as presence and amount of β-CD, use of other carbon sources and sintering times.

In the absence of β-CD, only irregular nanoparticles of NiO were formed by sintering $NiCl_2 \cdot 6H_2O$ (Fig. S4, ESI†). This implies the significant role of β-CD in creating the octahedral NiO structure. Similar phenomena also arose in research on polyhedral structures of other metal oxides.[30] In order to understand this role it is essential to know how the amount of β-CD influences the crystal growth of NiO.

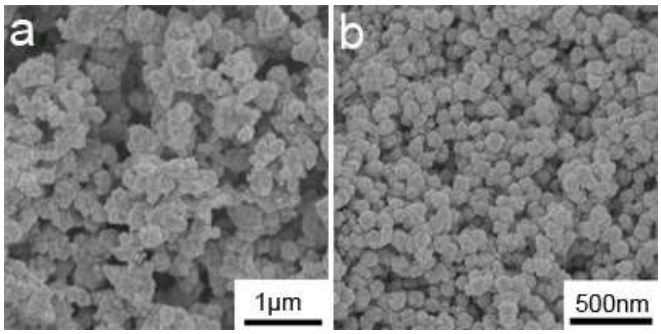

Fig. 3 FE-SEM images of NiO-**2** and NiO-**3**.

When the IMRs of $NiCl_2$ to β-CD in the precursors were decreased to 1:1 and 1:10, irregular structures of NiO (Fig. S5, ESI†) with different sizes (NiO-**2**, diameter: 150~200 nm; NiO-**3**, diameter: 100~150 nm) were obtained, as shown in Fig. 3. Again, for further information, it is worthy to mention that the particles in the NiO-**2** and NiO-**3** appear to be aggregates composed of many nanocrystals, and especially that the NiO-**3** particles clearly indicate an apparently homogeneous size distribution.

This result demonstrates two points. First, more addition of β-CD into the precursors will lead to the formation of NiO particles with smaller sizes. Second, the constructing of the octahedral NiO crystal needs the assistance of a suitable amount of β-CD. Indeed, we have no clear explanation for the two significant correlations. It is possible that they are related to the factors: i) an effect of the molecule-ion interaction between MCl_2 (M^{2+}, transition metallic ions) and β-CD in a precursor on the electrostatic interaction between M^{2+} and Cl^- ions,[31,32] causing a considerable change in the transformation temperatures from $NiCl_2$ to NiO (Fig. S6, ESI†); and ii) a contribution of carbon atoms in graphitic form (Fig. S7, ESI†) derived from the carbonization of β-CD to the preconcentration[33] and deposition rates[34] of NiO. The existence of carbon particles at an early stage of the calcination process was confirmed by both XRD patterns and Raman spectra (Fig. S7, ESI†). The former shows a broad diffraction peak centered at 21. 9° due to carbon particles, and the latter exhibits two strong Raman bands centered at 1387 (D band) and 1595 cm^{-1} (G band), implying the formation of carbon particles.[35] These suggestions are partially supported by additional experiments. For example, the stretching vibration band of OH groups in β-CD at 3452 cm^{-1} shows a clear red shift to 3392 cm^{-1} in the mixture of β-CD and $NiCl_2$ (Fig. S8, ESI†), suggesting that the hydrogen bonding interaction between β-CD molecules was weaken by the presence of $NiCl_2$. For another example, when β-CD was replaced by the other carbon sources such as active carbon and glucose, octahedral NiO crystals also can be produced at the same conditions, but the octahedra present the irregular growth and poor size distribution (Figs. S9 and S10, ESI†). It may be an indication that β-CD has a stronger effect on the close-packed structure of $NiCl_2$ generated in the crystallization process compared to the other two carbon sources. The result of conductivity measurements supports this: the molar conductivity of $NiCl_2$ was decreased in the order of β-CD > glucose > active carbon in solutions (Fig. S11, ESI†).

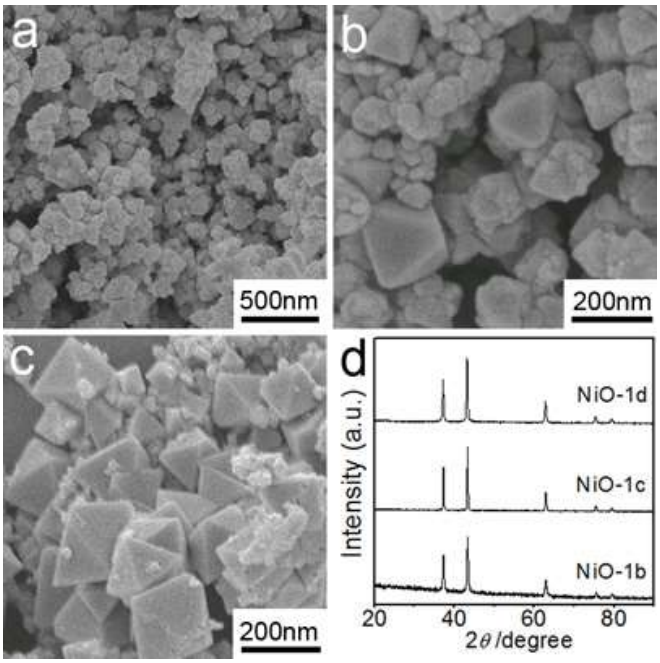

Fig. 4 FE-SEM images of NiO-**1b** (a), -**1c** (b) and -**1d** (c), and their XRD patterns (d).

These observations show that the morphology and size of the as-prepared NiO materials are not only strongly depended on the presence of β-CD during the sintering process, but also closely associated with the IMRs of $NiCl_2$ to β-CD in the precursors.

To determine the formation process of the fascinating NiO octahedra, a time-dependent growth experiment was carried out. Fig. 4 shows the SEM images XRD patterns of NiO-**1b**, -**1c** and -**1d**. Undoubtedly, the three samples are all pure NiO, based on their XRD

patterns (Fig. 4d). They can be regarded as the intermediates of the final product: NiO-**1a** octahedra. As can be seen from Fig. 4a, at the first stage of formation (2 h), the nanoparticles (NiO-**1b**, diameter: 50~100 nm) are indicated to be prone to form agglomeration. When the sintering time is increased to 4 h, there are several small octahedra with an edge length of about 100 nm (Fig. 4b). By further increasing the sintering time to 8 h, numerous particles with octahedral structures (edge length: 150~200 nm) were observed, as shown in Fig. 4c. At the final stage of formation (12 h), the octahedral particles become larger and more uniform in shape (see Fig. 2a). These observations provide the first direct evidence that the formation of the octahedral NiO structure undergoes a continuous transformation from irregular particles, small octahedra to big octahedral with the increase of sintering time, as illustrated in Fig. 5. The time-dependent structural evolution (from irregular nanoparticles to octahedral particles) and alteration (improvement of octahedral morphology) strongly implies that the parameter of sintering time can be used not only as an indication of determining the extent of crystal growth, but also as a tool to control the growth process for 3-dimension architectures.

Taken together, these results allow us to describe the formation process of the NiO octahedra by reactions 1~4. Initially, the thermal decomposition and carbonization of β-CD molecules in its mixture with $NiCl_2$ inevitably generate carbon dioxide, water, and carbon particles (Equations 1 and 2). It is remarkable to note that the carbon particles can only be seen in a very early stage (0.5 h) of sintering process, and no carbon signal was found after sintering for 1 h based on Raman analysis (Fig. S7, ESI†). Subsequently, a continuous reaction process (Equations 3 and 4, Fig. S4, ESI†) is involved in the creation of NiO crystals.

$$C_{42}H_{70}O_{35} + 42O_2 \xrightarrow{\Delta} 42CO_2 + 35H_2O \quad 1)$$

$$C_{42}H_{70}O_{35} \xrightarrow{\Delta} 42C + 35H_2O \quad 2)$$

$$NiCl_2 + 2H_2O \xrightarrow{\Delta} Ni(OH)_2 + 2HCl \quad 3)$$

$$Ni(OH)_2 \xrightarrow{\Delta} NiO + H_2O \quad 4)$$

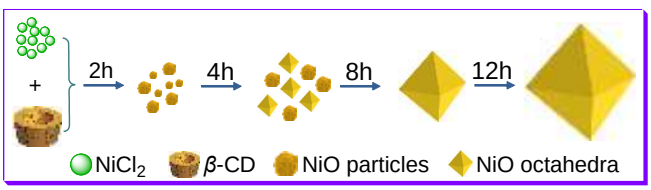

Fig. 5 Schematic illustration of the formation of the NiO octahedra.

Based on the results of control experiments, we deduce that the amount and form of carbon particles in the sintering system is a significant factor contributing to the growth and development of the NiO crystals, and the sintering time is the other key factor in controlling their morphologies and sizes. The former can be supported in part by Yuan and collaborators who described a strategy for the formation of single-crystalline hollow NiO octahedra using carbon spheres as templates.[36] The latter has been demonstrated by Tong and co-workers in the formation analysis of submicrometer-sized NiO octahedra generated through the thermal decomposition of $Ni(NO_3)_2{\cdot}6H_2O$.[37]

3. 3 Magnetic properties of NiO-1a and NiO-3

Fig. 6 displays the magnetization curve of the NiO octahedra by using SQUID magnetometry at 300 K. Obviously, this material has a very small hysteresis loop in a low field environment below 1 kOe at this temperature, showing ferromagnetic behaviour.

This result is considerably different from that of bulk NiO materials, as they generally show antiferromagnetic behaviour.[38,39] We consider that this ferromagnetic behavior could be associated with the inherent shape anisotropy seen in nanomaterials.[40] The unsaturated hysteresis loop also demonstrates the large anisotropy in the octahedra. The unsaturated magnetization at high fields may be due to the small grain size of this microstructure. The magnetization remanence and coercivity are estimated at about 4 memu·g^{-1} and 29.47 Oe, respectively, from the magnetic hysteresis loop. Meanwhile, as shown in Fig. S12, the NiO-**3** also shows the same ferromagnetic behaviour with an enhanced coercivity of 63.86 Oe and a high remanence of 13 memu·g^{-1}. In a word, the absence of the magnetization saturation for applied fields as large as 8 kOe seems to be characteristic of a superparamagnetic phase, but the existence of such a low remanence and coercivity is a direct proof of a small ferromagnetic contribution.

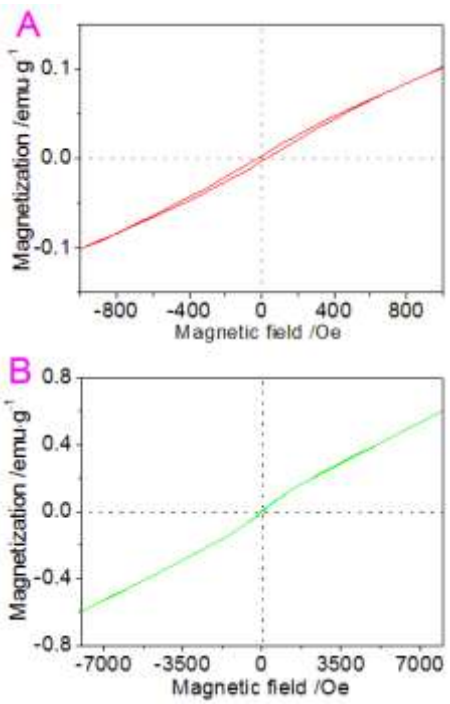

Fig. 6 Field dependence of magnetization of the NiO octahedra at 300 K in the applied fields: (A) from −1000 to 1000 Oe; (B) from −8000 to 8000 Oe.

3. 4 Lithium storage performances of NiO-1a and NiO-3

Nanostructured NiO including nanowalls,[41] nanorods[42] and nanospheres[43] is a promising anode material for lithium-ion batteries owing to its high theoretical capacity, high stability and low cost.[44,45] To the best of our knowledge, there are few published works on polyhedral NiO-lithium-ion battery systems. This urges us to consider the electrochemical performance of the NiO octahedra in order to make a comparison possible.

Fig. 7 shows the charge-discharge curves of two typical NiO materials: NiO-**1a** and NiO-**3** in the voltage range from 0.01 to 3.00 V at a constant current density of 100 mA·g^{-1}. The NiO-**1a** and NiO-**3** electrodes deliver discharge capacities of 1040, 794, and 759

mAh·g^{-1} and 840, 771, and 706 mAh·g^{-1} in the first, second, and third cycles, respectively. Clearly, their initial capacities are much higher than the theoretical capacity (718 mAh·g^{-1}) for bulk NiO. The extra capacity could be resulting from the formation of the solid–electrolyte interface layer. Similar phenomena were observed in many metal oxides such as Fe_2O_3,[46] Co_3O_4[47] and TiO_2.[48] This result indicates that the NiO-**1a** and NiO-**3** exhibit high lithium storage capability. Also, we noticed that the initial capacities are much lower than those of nanoflowers,[49] nanosheets[26] and nanowires.[27] A possible reason may be the relatively large grain size. Additionally, there is a drastic decrease to below 85% of the initial capacity in the subsequent two cycles for the octahedral NiO electrode, but such a decrease was not observed for the NiO-**3** electrode. Thus, it is obvious that the NiO-**3** with smaller grain sizes seems to be a better electrode material than the octahedral NiO for the present application. The discharge potential plateaus at 0.45~0.65 V in the first discharge process can be attributed to the following reaction:[50]

$$NiO + 2Li^+ + 2e^- \longrightarrow Ni + Li_2O \qquad 5)$$

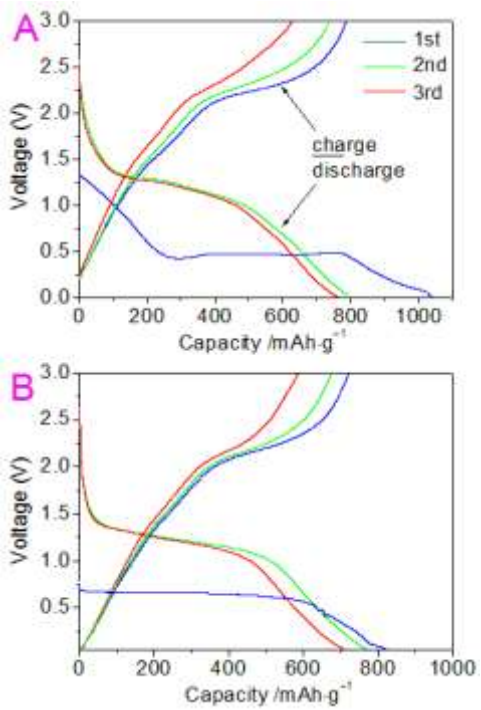

Fig. 7 Charge-discharge voltage profiles of (A) the NiO octahedra and (B) the NiO-**3** for the first three cycles at a current density of 100 mA·g^{-1}.

It is important to note the very low irreversible capacity loss (less than 5%) on the NiO-**3** during the first three cycles. This result is comparable with those achieved with nanotubes,[51] nanosheets[52] and nanoplatelets[53] with relatively small size.

Fig. 8 shows the cycle performance and coulombic efficiency of the NiO-**3** at a current density of 100 mA·g^{-1}. After 28 cycles, the reversible capacity for this material is still as high as 458 mAh·g^{-1}, which is much higher than the theoretical specific capacity of graphite (372 mAh·g^{-1}) and the NiO octahedra (380 mAh·g^{-1}, Fig. S13, ESI†). In particular, this battery shows sufficient high

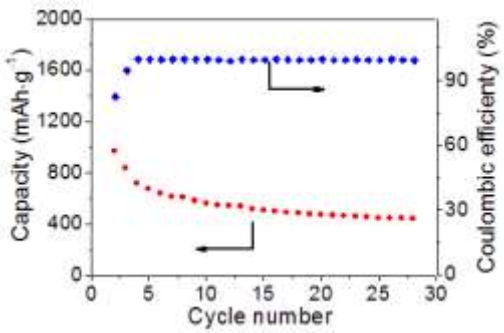

Fig. 8 Cycling performance and coulombic efficiency of the NiO-**3** at a current density of 100 mA·g^{-1}.

coulombic efficiency (higher than 99%), even after 28 charge-discharge cycles.

These observations suggest that the NiO-**3** with a relatively higher electrochemical performance than the NiO octahedra is a promising anode material for lithium-ion batteries due to high lithium storage capability, very low irreversible capacity loss and good cyclability.

4. Conclusions

In this work, we developed a new facile synthesis procedure for preparation of NiO octahedra and agglomerates by simply sintering the binary mixtures of $NiCl_2$ with β-CD without using any templates and organic solvents. The composition of the binary mixtures is one important factor in the control of the morphology and microstructure of NiO. The other important factor is sintering time. The studies presented in this paper allow us, for the first time, to compare the difference in electrochemical properties of the octahedral structure and agglomerate structure of NiO. Our results revealed that the NiO-**3** agglomerates with smaller grain sizes shows a relatively higher performance for lithium storage compared to the octahedra, for example, high lithium storage capability, low irreversible capacity loss and good cycling performance. Hence, it is hoped that this work will be useful not only for a better understanding of the design and fabrication process of transition metal oxide materials but also for understanding the relationship between the microstructure and electrochemical function of the materials.

Acknowledgements

The authors are grateful to NSFC of China (No. 21071139) for financial support of this work.

Supporting Information Available

1) EDS spectra of the NiO-**1b** and NiO-**3**; 2) FE-SEM images of NiO-**1a** obtained by sintering the intimate mixtures of $NiCl_2$ and β-CD with the IMR of 1:0.1 ($NiCl_2$-β-CD-**a**) for 12 h at 773 K; 3) FE-SEM image and XRD pattern of the NiO material by sintering $NiCl_2 \cdot 6H_2O$ at 773 K for 12 h; 4) The XRD patterns of the NiO-**2** (A) and NiO-**3** (B). 5) TG profiles of $NiCl_2 \cdot 6H_2O$, $NiCl_2$-β-CD-**a**, $NiCl_2$-glucose and $NiCl_2$-carbon in air at a heating rate 10.0 K·min^{-1}; 6) XRD patterns and Raman spectra of the sintering products of $NiCl_2$-β-CD-**a** at 773 K for 0.5 and 1 h; 7) FTIR spectra of β-CD and $NiCl_2$-β-CD-**a**; 8) FE-SEM images and XRD patterns of NiO-**4** and NiO-**5**; 9) Molar conductivity of the $NiCl_2$ solutions in the presence

of β-CD, glucose and carbon with the IMR values from 0 to 10; 10) Field dependence of magnetization of the NiO agglomerates at 300 K and 11) Cycling performance and coulombic efficiency of the NiO octahedra are available free of charge via the Internet at http://www.rsc.org.

References

1 S. Seo, M. Lee, D. Seo, E. Jeoung, D.-S. Suh, Y. Joung, I. Yoo, I. Hwang, S. Kim and I. Byun, *Appl. Phys. Lett.*, 2004, **85**, 5655..

2 M. Ghosh, K. Biswas, A. Sundaresan and C. Rao, *J. Mater. Chem.*, 2006, **16**, 106.

3 J. Park, E. Kang, S. U. Son, H. M. Park, M. K. Lee, J. Kim, K. W. Kim, H. J. Noh, J. H. Park and C. J. Bae, *Adv. Mater.*, 2005, **17**, 429.

4 D. P. Chen, X. L. Wang, Y. Du, S. Ni, Z. B. Chen and X. Liao, *Cryst. Growth Des*., 2012, **12**, 2842.

5 (a) S. A. Needham, G. Wang and H. K. Liu, *J. Power Sources*, 2006, **159**, 254. (b) H. Pang, Q. Lu, Y. Li and F. Gao, *Chem. Commun.*, 2009, **48**, 7542.

6 Q. Yang, J. Sha, X. Ma and D. Yang, *Mater. Lett*., 2005, **59**, 1967.

7 H. Wu, M. Xu, H. Wu, J. Xu, Y. Wang, Z. Peng and G. Zheng, *J. Mater. Chem.*, 2012, **22**, 19821.

8 D. Wang, R. Xu, X. Wang and Y. Li, *Nanotechnology*, 2006, **17**, 979.

9 (a) S. Xing, Q. Wang, Z. Ma, Y. Wu and Y. Gao, *Mater. Res. Bull*., 2012, **47**, 2120. (b) T. Zhu, J. S. Chen and X. W. Lou, *J. Phys. Chem. C*, 2012, **116**, 6873.

10 M. A. Ali, P. R. Solanki, M. K. Patel, H. Dhayani, V. V. Agrawal, R. John and B. D. Malhotra, *Nanoscale*, 2013, **5**, 2883.

11 Y. Cui, C. Wang, S. Wu, G. Liu, F. Zhang and T. Wang, *CrystEngComm*, 2011, **13**, 4930.

12 P. Justin, S. K. Meher and G. R. Rao, *J. Phys. Chem. C*, 2010, **114**, 5203.

13 X. Song and L. Gao, *J. Am. Ceram. Soc*., 2008, **91**, 3465.

14 X. Xia, J. Tu, Y. Zhang, J. Chen, X. Wang, C. Gu, C. Guan, J. Luo and H. J. Fan, *Chem. Mater*., 2012, **24**, 3793.

15 C. Wang, H. Wu, Z. Chen, M. T. McDowell, Y. Cui and Z. Bao, *Nat.. Chem.*, 2013, **5**, 1042.

16 E. Yoo, J. Kim, E. Hosono, H.-S. Zhou, T. Kudo and I. Honma, *Nano Lett*., 2008, **8**, 2277.

17 (a) L. Yu, Z. Wang, L. Zhang, H. B. Wu and X. W. D. Lou, *J. Mater. Chem. A*, 2013, **1**, 122. (b) J. Xu, C. Jia, B. Cao and W. Zhang, *Electrochim. Acta*, 2007, **52**, 8044.

18 (a) X. Rui, Z. Lu, H. Yu, D. Yang, H. H. Hng, T. M. Lim and Q. Yan, *Nanoscale*, 2013, **5**, 556. (b) Z. l. Wang, D. Xu, L. M. Wang and X. B. Zhang, *ChemPlusChem*, 2012, **77**, 124. (c) T. Puangpetch, S. Chavadej and T. Sreethawong, *Powder Technol.*, 2011, **208**, 37.

19 (a) L. Q. Mai, B. Hu, W. Chen, Y. Qi, C. Lao, R. Yang, Y. Dai and Z. L. Wang, *Adv. Mater.*, 2007, **19**, 3712. (b) Z. Wang, S. Madhavi and X. W. Lou, *J. Phys. Chem. C*, 2012, **116**, 12508.

20 (a) X. W. Lou, D. Deng, J. Y. Lee and L. A. Archer, *J. Mater. Chem*., 2008, **18**, 4397. (b) X. W. Lou, D. Deng, J. Y. Lee, J. Feng and L. A. Archer, *Adv. Mater*., 2008, **20**, 258. (c) X. Y. Xue, S. Yuan, L. L. Xing, Z. H. Chen, B. He and Y. J. Chen, *Chem. Commun*., 2011, **47**, 4718.

21 (a) H. B. Wu, J. S. Chen, H. H. Hng and X. W. Lou, *Nanoscale*, 2012, **4**, 2526. (b) J. Jiang, Y. Y. Li, J. P. Liu, X. T. Huang, C. Z. Yuan and X. W. Lou, *Adv. Mater.*, 2012, **24**, 5166. (c) Z. Y. Wang, L. Zhou and X. W. Lou, *Adv. Mater.*, 2012, **24**, 1903.

22 F. Cao, F. Zhang, R. Deng, W. Hu, D. Liu, S. Song and H. Zhang, *CrystEngComm*, 2011, **13**, 4903.

23 J. H. Pan, Q. Huang, Z. Y. Koh, D. Neo, X. Z. Wang and Q. Wang, *ACS Appl. Mater. Inter.*, 2013, **5**, 6292.

24 Y. Zou and Y. Wang, *Nanoscale*, 2011, **3**, 2615.

25 X. Wang, L. Qiao, X. Sun, X. Li, D. Hu, Q. Zhang and D. He, *J. Mater. Chem. A*, 2013, **1**, 4173.

26 A. K. Mondal, D. Su, Y. Wang, S. Chen and G. Wang, *Chem. Asian J*., 2013, **8**, 2828.

27 D. Su, H. S. Kim, W. S. Kim and G. Wang, *Chem. Eur. J*., 2012, **18**, 8224.

28 C. Jiang, Y. Han, S. Liu and Z. Zhang, *CrystEngComm*, 2014, **16**, 952.

29 L. X. Song, Z. K. Yang, Y. Teng, J. Xia and P. Du, *J. Mater. Chem. A*, 2013, **1**, 8731.

30 L. B. Wang, L. X. Song, Z. Dang, J. Chen, J. Yang and J. Zeng, *CrystEngComm*, 2012, **14**, 3355.

31 L. X. Song, S. Z. Pan, L. H. Zhu, M. Wang, F. Y. Du and J. Chen, *Inorg. Chem.*, 2011, **50**, 2215

32 J. Yang, L. X. Song, J. Yang, Z. Dang and J. Chen, *Dalton Trans*., 2012, **41**, 2393.

33 F. Giordano, C. Novak and J. R. Moyano, *Thermochim. Acta*., 2001, **380**, 123.

34 F. Trotta, M. Zanetti and G. Camino, *Polym. Degrad. Stabil*., 2000, **69**, 373.

35 a) L. X. Song, M. Wang, S. Z. Pan, J. Yang, J. Chen and J. Yang, *J. Mater. Chem.*, 2011, **21**, 7982. b) J. Xia, L. X. Song and Z. Dang, *J. Phys. Chem. B*, 2012, **116**, 7635.

36 X. Wang, L. Yu, P. Hu and F. Yuan, *Cryst. Growth Des*., 2007, **7**, 2415.

37 G. Tong, Q. Hu, W. Wu, W. Li, H. Qian and Y. Liang, *J. Mater. Chem*., 2012, **22**, 17494.

38 R. W. Chantrell, M. El-Hilo and K. O'Grady, *IEEE Trans. Magn.*, 1991, **27**, 3570.

39 P. Ngo, P. Bonville and M. P. Pileni, *Eur. Phys. J. B*, 1999, **9**, 583.

40 Y. W. Jun, J. w. Seo and J. Cheon, *Accounts Chem. Res*., 2008, **41**, 179.

41 B. Varghese, M. Reddy, Z. Yanwu, C. S. Lit, T. C. Hoong, G. Subba Rao, B. Chowdari, A. T. S. Wee, C. T. Lim and C. H. Sow, *Chem. Mater.*, 2008, **20**, 3360.

42 Y. Zou and Y. Wang, *Rare Metals*, 2011, **30**, 59.

43 (a) G. Zhang, Y. Chen, B. Qu, L. Hu, L. Mei, D. Lei, Q. Li, L. Chen, Q. Li and T. Wang, *Electrochim. Acta*, 2012, **80**, 140. (b) A. K. Mondal, D. Su, Y. Wang, S. Chen, Q. Liu and G. Wang, *J. Alloy Compd.*, 2014, **582**, 522.

44 A. K. Mondal, D. Su, Y. Wang, S. Chen, Q. Liu and G. Wang, *J. Alloy. Compd*., 2014, **582**, 522.

45 L. Zhuo, Y. Wu, W. Zhou, L. Wang, Y. Yu, X. Zhang and F. Zhao, *ACS Appl. Mater. Inter.*, 2013, **5**, 7065.

46 C. Li, X and D. Lou, *Chem. Commun*., 2011, **47**, 8061.

47 C. Li, X. Yin, L. Chen, Q. Li and T. Wang, *Chem. Euro. J*., 2010, **16**, 5215.

48 H. Han, T. Song, J.-Y. Bae, L. F. Nazar, H. Kim and U. Paik, *Energ. Environ. Sci*., 2011, **4**, 4532.

49 C. Zhang, J. Chen, Y. Zeng, X. Rui, J. Zhu, W. Zhang, C. Xu, T. M. Lim, H. H. Hng and Q. Yan, *Nanoscale*, 2012, **4**, 3718.

50 G. Zhang, Y. Chen, B. Qu, L. Hu, L. Mei, D. Lei, Q. Li, L. Chen, Q. Li and T. Wang, *Electrochim. Acta*, 2012, **80**, 140.

51 S.A. Needham, G.X. Wang and H.K. Liu, *J. Power Source*, 2006, **159**, 254.

52 X. Wang, L. Qiao, X. Sun, X. Li, D. Hu, Q. Zhang and D. He, *J. Mater. Chem. A*, 2013, **1**, 4173.

53 X. Wang, L. Li, Y. g. Zhang, S. Wang, Z. Zhang, L. Fei and Y. Qian, *Cryst. Growth Des*., 2006, **6**, 2163

PAPER www.rsc.org | CrystEngComm

Synthesis and Lithium Storage Performance of Nickel Oxide Octahedra

Zheng Kun Yang, Le Xin Song*, Rong Rong Xu, Yue Teng, Juan Xia, Li Zhao and Qing Shan Wang

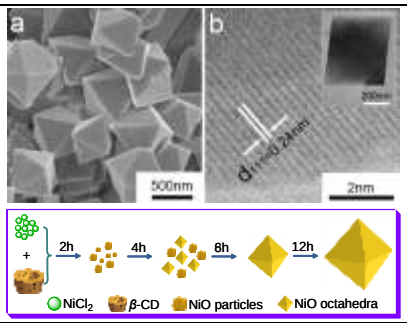

Octahedral NiO crystals obtained by a facile synthesis route show high performance for lithium storage